Tailoring Co3d and O2p band centers to inhibit oxygen escape for stable 4.6V $LiCoO_2$ cathodes

Weijin Kong[a], Jicheng Zhang[a], Deniz Wong[b], Wenyun Yang[c], Jinbo Yang[c], Christian Schulz[b] and Xiangfeng Liu[a,d]*

[a] Center of Materials Science and Optoelectronics Engineering, College of Materials Science and Optoelectronic Technology, University of Chinese Academy of Sciences, Beijing 100049, P. R. China

[b] Helmholtz-Center Berlin for Materials and Energy, Hahn-Meitner-Platz 1, Berlin 14109, Germany

[c] State Key Laboratory for Mesoscopic Physics, School of Physics, Peking University, Beijing 100871, China

[d]CAS Center for Excellence in Topological Quantum Computation, University of Chinese Academy of Sciences, Beijing 100190, China

*Corresponding Author: liuxf@ucas.ac.cn. (X.L.) Tel. +86 10 8825 6840

Abstract

High voltage $LiCoO_2$ delivers a high capacity but sharp fading is a critical issue, and the capacity decay mechanism is also poorly understood. Herein, we clarify that the escape of surface oxygen and Li-insulator Co_3O_4 formation are the main causes for the capacity fading of 4.6V $LiCoO_2$. We further propose the inhibition of the oxygen escape for achieving stable 4.6V $LiCoO_2$ by tailoring the Co3d and O2p band center and enlarging their band gap with MgF_2 doping. This enhances the ionicity of the Co-O bond and the redox activity of Co, and improves cation migration reversibility. Moreover, the inhibition of oxygen escape suppresses the formation of Li-insulator Co_3O_4 and maintains the surface structure integrity. Mg acts as a "pillar", providing a stable and enlarged channel for fast Li^+ intercalation/extraction. The modulated $LiCoO_2$ shows almost "zero strain" and achieves a record capacity retention at 4.6V: 92% after 100 cycles at 1C and 86.4% after 1000 cycles at 5C. This work offers some insights into modulating the local electronic structure for high-voltage $LiCoO_2$.

Key words: high voltage $LiCoO_2$; oxygen release; band center; energy gap; MgF_2 doping

TOC

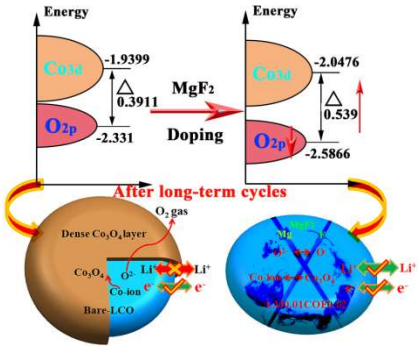

We report that the escape of surface oxygen and Li-insulator Co_3O_4 formation are the main causes for the capacity fading of 4.6V $LiCoO_2$ cathode. The oxygen escape is significantly inhibited by tailoring the Co3d and O2p band centers and enlarging their band gap with MgF_2 doping, which enables a stable cycling of 4.6V $LiCoO_2$ cathode.

1. Introduction

Since its commercialization in 1991, lithium-ion batteries (LIBs) have become the preferred energy storage systems for portable electronic products and electric vehicles[1]. However, the development of LIBs has fallen far behind the increasing demand for high-energy density batteries [2]. As the pioneering cathode material of rechargeable lithium-ion batteries, $LiCoO_2$ (LCO) is still dominant in 3C electronic devices due to its high tap density [3]. However, the capacity of the widely used LCO is approximately 140mAh/g, which means that only half of the Li^+ is extracted from LCO. A high cutoff voltage can result in a large capacity, but it is accompanied by sharp capacity fading [4]. In recent decades, some modification strategies have been reported to enhance the cycling stability of $LiCoO_2$ at a high voltage. For example, Li et al enhanced the capacity retention of 4.6V $LiCoO_2$ to 86% at 0.5C through Ti-Mg-Al co-doping[5]. Lu et al reported a class of ternary lithium, aluminum and fluorine-modified $LiCoO_2$ with a stable and conductive layer [6]. Li et al improved the cycling stability through Se substitution(Se-LCO), and Se-LCO retained 80% of its capacity after 450 cycles at 100 mA g^{-1} in 4.57 V pouch full cells[7]. Recently, Huang et al reported a 4.6V Mg-pillared $LiCoO_2$ with a capacity retention of 84% at 1.0 C over 100 cycles [8]. However, improving the long-term cycling stability of $LiCoO_2$ at a high voltage of 4.6V is still a great challenge.

Additionally, the charge compensation and capacity degradation mechanism of high voltage $LiCoO_2$ are still not very clear. Pan et al reported that the structural stability was related to the flatness of $LiCoO_2$ layers [9]. However, there are still some issues that

have not been well understood. It has been reported that oxygen redox ($O^{2-} \leftrightarrow O_2^{n-}$) begins to contribute to capacity at a higher voltage due to O_{2p} orbital hybridization with the Co_{3d} orbital in the $Co^{3+/4+}$:t_{2g} and O_{2p} resonant bands at lower electronic energies[10]. The electrons are extracted from both Co^{3+} and O^{2-}, which leads to O^{2-} oxidation and oxygen loss from the cathode materials due to the decrease in the ion radius and electrostatic force, especially at a high potential[7, 11],[12]. Moreover, the formed oxygen, including O_2 gas and O^- radicals is highly oxidizing, which rapidly decomposes the carbonate electrolyte and produces a thick cathode electrolyte interface (CEI) that affects the cycling performance of the batteries. Some groups have reported that when LCO cathode material is charged to a high voltage, it undergoes a harmful phase transition from the O3 hexagonal phase to the hybrid O1-O3 hexagonal phase, which is accompanied by sliding and partial collapse of the O3 lattice plate[5, 13]. The oxygen redox at a high voltage affects the structural stability of $LiCoO_2$. Subsequently, the increase in the internal crystal lattice stress in $LiCoO_2$ results in the formation of cracks and particle crushing [14]. Regardless, it is quite important to clarify the degradation mechanism of high voltage $LiCoO_2$ and find a facile strategy to fundamentally address capacity fading.

In this work, we propose the suppression of the oxygen escape and cation migration by lowering the Co3d and O2p band centers and enlarging their band gap with MgF_2 doping. This enhances the ionicity of the Co-O bonds, improves the stability of the layered structure and inhibits the formation of the Li^+-insulator Co_3O_4 on the surface of $LiCoO_2$. The long-term cycling stability and rate capability are both

significantly improved. Neutron powder diffraction (NPD), operando differential electrochemical mass spectrometry (DEMS), soft resonance inelastic X-ray scattering (RIXS), High-angle annular dark field scanning transmission electron microscopy (HAADF-STEM) and first principles calculations (DFT) are applied to probe the modification mechanism. Different from the previous viewpoints, we also find that oxygen escape and the resulting formation of Li^+-insulator Co_3O_4 on bare $LiCoO_2$ at 4.6V are the main causes of the sharp capacity decay. Our findings show that tuning the energy gap between the Co3d and O2p band centers offers a feasible strategy to fundamentally solve the issues of oxygen release and cationic migration for high voltage $LiCoO_2$, which may be extended to other oxygen redox-related cathode materials.

2. Result and Discussion

Crystal structure and Morphology

To analyze the layered crystal structures of the Bare-LCO, LM0.01COF0.02, LM0.01CO, LCOF0.02, LM0.02COF0.04, and LM0.03COF0.06 samples, X-ray diffraction (XRD) patterns were collected as shown in Figure 1 (a) and Figure S1 (a), and neutron powder diffraction (NPD) data of the Bare-LCO and LM0.01COF0.02 samples were collected as shown in Figure S2 (a). As expected, the Bare-LCO sample has a pure crystal structure and can be described with all the peaks indexed to the layered α -$NaFeO_2$ structures in the R $\bar{3}$ m space group symmetry[15]. The LM0.01COF0.02 sample still maintains a layered structure without any impurity peak. Figure 1 (b) and Figure S1 (b) show the Rietveld refinement of the XRD patterns of the

Bare-LCO and LM0.01COF0.02 cathode materials, respectively, and the refined crystallographic parameters are listed in Table 1(by XRD) and Table 2(by NPD), which indicate that the rule and trend of refined XRD data are consistent with those of the NPD data. The occupancy information of the atoms in cathode materials from the Rietveld refinement is depicted in Tables S1~S4. The fitting factors R_{wp} are 2.42 and 2.26%, respectively, which mean that the refined data are acceptable for further reference.

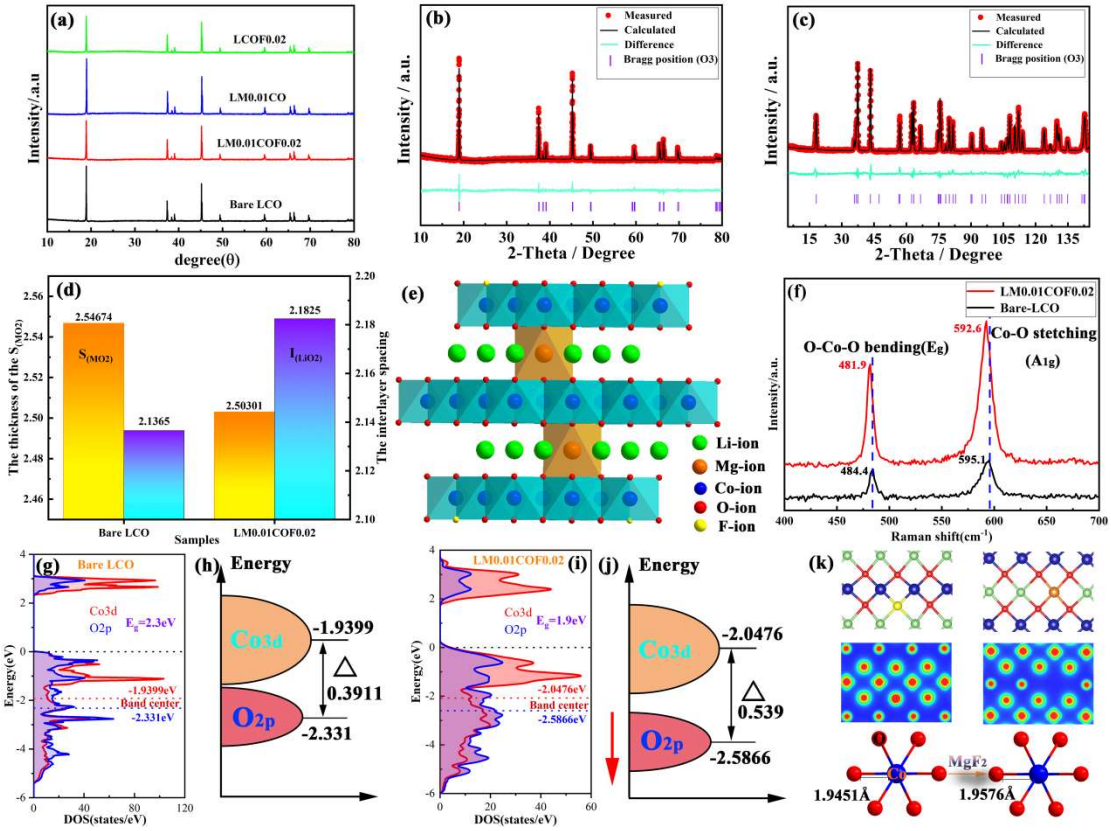

Figure 1. (a) The XRD patterns; the refinement results of the materials (b) LM0.01COF0.02; and the refinement results of the neutron powder diffraction (NPD), (c) LM0.01COF0.02, (d) is the comparison of the thickness of the $S_{(MO2)}$ and the interlayer spacing of the refinement results; (e) the Refined crystal structures of the LM0.01COF0.02 by the NPD, (f) the Raman patterns of the Bare LCO and LM0.01COF0.02, the calculated density of states: (g) Bare LCO, (i) LM0.01COF0.02, (h)

and (j) diagram of the energy gap between Co3d and O2p band center, (k) calculation of the influence on the electron distribution of oxygen elements by the MgF_2 doping and the length of the Co-O band.

Moreover, compared with Bare-LCO (2.54674 Å), the thickness of $S_{(MO2)}$ for LM0.01COF0.02 decreased to 2.50301 Å after MgF_2 co-doping as shown in Figure 1 (d), which illustrates the enhanced stability of the layered structure. There are many factors affecting Li^+ migration, the most important of which is the interlayer spacing $Li_{(LiO2)}$. The increase in $Li_{(LiO2)}$ can provide a wider channel for Li^+ intercalation/extraction during the charge/discharge processes, which lower the energy barrier and lower the resistance of Li^+ migration. The expansion of $Li_{(LiO2)}$ in LM0.01COF0.02 is larger than that in Bare-LCO cathode materials as shown in Figure 1 (d), which indicates that Mg ions enter the Li site successfully, and can provide a stable and enlarged channel for fast Li^+ intercalation/extraction. Because the electronegativity of F^- is stronger than that of O^{2-}, thus being more attractive to electrons, both the reduced thickness of $S_{(MO2)}$ and the expansion of $Li_{(LiO2)}$ have a profound influence on the structural stability and migration of Li^+ ions in cathode materials.

The crystal structure of the modified LCO sample based on the Rietveld refinement of the NPD pattern is shown in Figure 1(e). The Mg at the Li site provides a “pillar” for lithium-ion migration, which can significantly enhance the structural stability. In addition, substituting F for oxygen benefits the stability of the O-ion due the F-ion being more electronegativity than O. The anti-3d orbital of Co is more stable

owing to presence of more Co-F ionic bonds, which can reduce the redox energy of Co ions to a favorable level (compared with the Fermi level of the lithium anode), and then reduce the hybridization of the Co_{3d} and O_{2p} orbitals, which further improves the structural stability. There are two paths for the Li-ion migration in $LiCoO_2$ cathode materials, as shown in Figure S3. Moreover, two typical vibrations are observed at Raman shifts of approximately 485 and 595 cm^{-1}, which can be attributed to O-Co-O bending (Eg) and Co-O stretching (A1g) in $LiCoO_2$, respectively, as shown in Figure 1(f). Compared with the strong Raman bonds observed at approximately 484.4 and 595.1 cm^{-1} for the Bare-LCO sample, the bonds in the LM0.01COF0.02 sample are at approximately 481.9 and 592.6 cm^{-1}, which means that all samples have a layered structure with the $R\bar{3}m$ space group and is consistent with the XRD and NPD patterns. However, the shift of the strong Raman bonds to the left for the LM0.01COF0.02 sample indicates the existence of lithium vacancies due to the substitution of Mg^{2+} for Li^{+}, which also confirms that Mg^{2+} occupies the Li site.

For $LiCoO_2$ cathode materials, with continuous increase of the charging voltage, the electrons lost in the cathode materials will gradually increase. This process will gradually lead to the depletion of valence band top of Co element higher than O2p orbit of oxygen element. After the depletion of valence band top electrons, the charge compensation process in this region will no longer be provided by transition metal elements alone, and anionic oxygen is also involved. To further find evidence of band gap broadening, first principles calculations (DFT) were carried out as shown in Figure 1(g)~(j). Compared with the Bare-LCO sample, the band gaps of LM0.01COF0.02

cathode material decreases from 2.3eV to 1.9eV, which can improve the electrical conductivity and further facilitate charge transfer for rapid kinetics. To some extent, the size of the energy gap between the transition metal and oxygen band centers reflects the covalent and ionic strength of the TM-O bonds[16]. Moreover, in Figure 1 (h) and (j), MgF_2 doping increases the energy gap between the O2p and Co3d band centers (△ from 0.3911eV to 0.539eV), resulting in lower oxygen redox activity and increasing Co-O bond ionicity. This can be quantified by the large energy band gap of the O2p and Co3d or the lower O2p band center position relative to the Fermi level, which can inhibit the activity of oxygen redox and enhance the ionic characteristic of the Co-O band due to the strong electronegativity of F and the immobilization function of oxygen by Mg. Compared with Bare-LCO (1.9451 Å), the length of the Co-O bond in the LM0.01COF0.02 (1.9576 Å) sample becomes longer, which is consistent with the increasing energy gap between the Co_{3d} and O_{2p} band centers. In addition, MgF_2 doping not only affects the change in the band gap but also has a certain effect on the electron cloud of oxygen ions. The intuitive change is the bond length of the Co-O bond as shown in Figure 1 (k). The decrease in the O2p band center significantly inhibits the oxygen redox activity in the bulk structure during Li insertion/extraction, which illustrates the enhanced structural stability of the LM0.01COF0.02 sample.

Table 1 the refined crystallographic parameters of the cathode materials by the XRD patterns.

Sample	a(Å)	c(Å)	V(Å^3)	Z_{ox}	TM-O	$S_{(MO2)}$(Å)	$I_{(LiO2)}$(Å)	R_{wp}(%)
Bare-LCO	2.8156(0	14.0498(5	96.46(0	0.2427(6	1.945	2.54674	2.1365	2.42

	)	)	)	)	1			
LM0.01COF0.02	2.8150(1)	14.0566(6)	96.47(0)	0.2443(5)	1.957 6	2.50301	2.1825	2.26

Table 2 The refined crystallographic parameters of the cathode materials by the NPD patterns.

Sample	a(Å)	c(Å)	V(Å^3)	Z_{ox}	TM-O	$S_{(MO2)}$(Å)	$I_{(LiO2)}$(Å)	R_{wp}(%)
Bare-LCO	2.8166(0)	14.0544(2)	96.56(0)	0.2395(6)	1.921 6	2.63698	2.0478	5.79
LM0.01COF0.02	2.8165(1)	14.0684(3)	96.65(0)	0.2408(3)	1.921 9	2.60359	2.0859	6.96

The morphology and crystal structure were further investigated by high-resolution transmission electron microscopy (HRTEM) as shown in Figure S4 (a) and (c). Both the Bare-LCO and LM0.01COF0.02 samples exhibit a similar micromorphology, and the selected electron diffraction spots and electron diffraction spots along the [104] and [003] zone axes of $R\bar{3}m$ from the Bare-LCO and LM0.01COF0.02 particles show significantly structural consistency[4b, 17]. To directly observe the distribution of each element in the LM0.01COF0.02 sample, EDS mapping spectra were obtained for verification as shown in Figure S4 (e)~(i), and Mg, Co, O and F are shown in Figure S4 (f)~(i), respectively. Overall, Mg and F are uniformly distributed in the LM0.01COF0.02 sample, which illustrates that the Mg and F are successfully doped into the host structure. In order to prove that the F^- dopes into the bulk phase, the depth

analysis of XPS was also performed as shown in Figure S5. There is still a strong signal of F^- when the sample is etched to about 50nm, which indicates that there is F element in the bulk phase. Therefore, after combining the XRD, NPD and HRTEM techniques, it is confirmed that two materials have a similar crystal structure and morphology.

Electrochemical performances and mechanisms

To evaluate the electrochemical performance of the samples, the kinetics and phase transition of Bare-LCO and LM0.01COF0.02 were studied by the cyclic voltammetry (CV) as shown in Figure 2 (a) and (b). The peaks at approximately 4.4V and 3.8V correspond to the phase transitions of M2/H3 and H2/H1, respectively. The characteristic of the order/disorder phase transition occurs near approximately 4.0 and 4.1V. With an increase in the number of scanning cycles, the peaks of the Bare-LCO samples gradually weaken, and the polarization phenomenon is obviously increases, which indicates that the phase transitions of M2/H3 and H2/H1 are irreversible due to the irreversible redox reaction of more oxygen and release O_2 gas during the Li insertion/extraction process. In contrast, the increasing sharp peaks of Co redox and the weak polarization of LM0.01COF0.02 mean that the redox activity of Co is further enhanced after activation, which confirms the enhanced of the structural reversibility and stability of the LM0.01COF0.02 cathode at high voltages, especially at 4.6V.

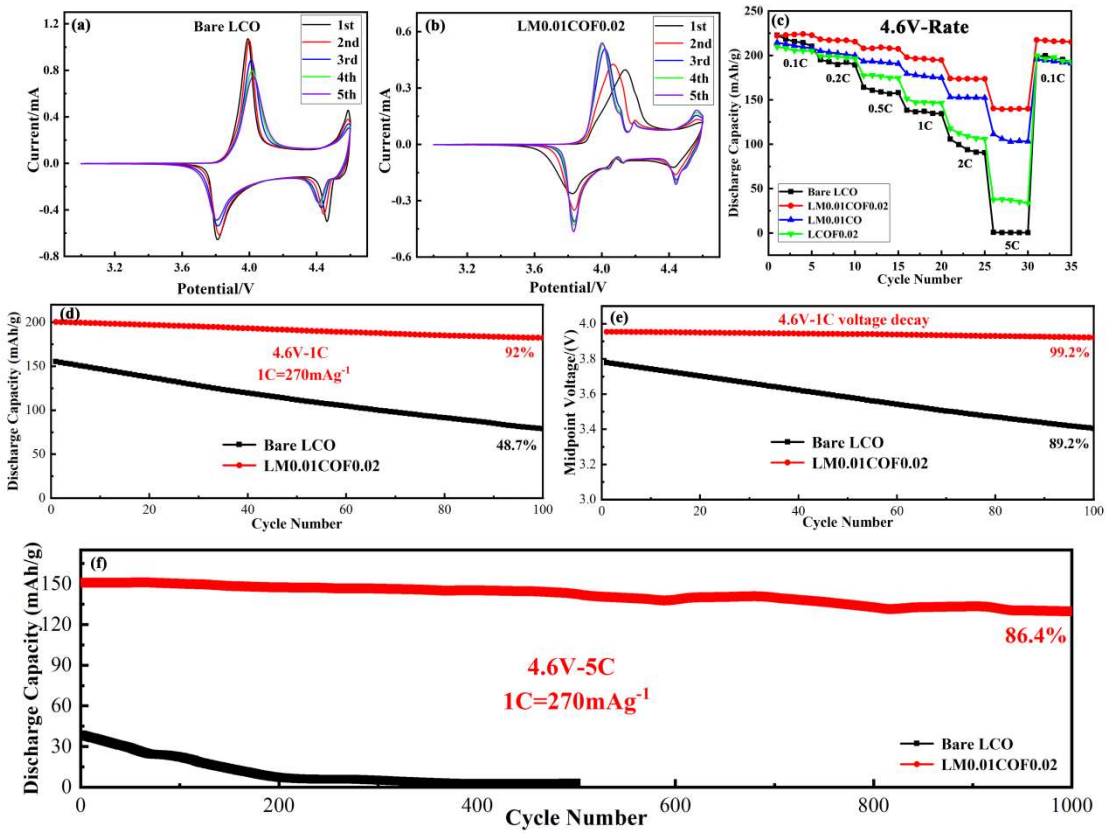

Figure 2 The Cyclic Voltammetry (CV) curves of as-prepared electrode materials with the scan rate of 0.1mV/s from 3.0V to 4.6V: (a) Bare LCO, (b) LM0.01COF0.02; (c) Rate capabilities test at different current densities (Bare LCO, LM0.01COF0.02, LM0.01CO, LCOF0.02; 1C = 270 mA g^{-1}), (d) cycling performance and coulomb efficiency, (e) voltage decay at 1C, (f) cycling performance at 5C.

As shown in Figure 2 (c), the rate performance of the Bare-LCO, LM0.01COF0.02, LM0.01CO and LCOF0.02 cathode materials were investigated in a range of 3.0V~4.6V. The LM0.01COF0.02 cathode material shows excellent rate performance, delivering capacities of 222, 218, 208, 198, 174 and 140mAh/g at 0.1C, 0.2C, 0.5C, 1C, 2C and 5C (1C=270mA/g), respectively, and recovering to 218mAh/g after the current density decreases back to 0.1C with a capacity retention of>97.9%. In contrast, the

Bare-LCO samples show a worse rate capacity with corresponding discharging capacities of 223, 195, 164, 138, 106 and 0.8mAh/g at 0.1C, 0.2C, 0.5C, 1C, 2C and 5C, respectively, and recovering to only 199mAh/g when going back to 0.1C and demonstrating a capacity retention of<89.2%. The charge/discharge curves of both samples are shown in Figure S6 (a) and (b). The improvement in rate capacity benefits from the expansion of the interlayer $I_{(LiO2)}$ in the host structure because the doping of Mg into the Li site can provide a "pillar" for the rapid migration of Li ions[8]. The stronger electronegativity of F than O can inhibit oxygen redox and significantly enhance the structural stability[18].

The electrochemical cycling performance of the $LiCoO_2$ cathode material in a Li half -cell at 1C is shown in Figure 2(d) and (e), which show the typical capacity decay and voltage decay during long-term cycling, respectively. Compared with the Bare-LCO samples, the capacity retention of the LM0.01COF0.02 samples was significantly improved from 48.7% to 92% after 100 cycles at 1C (1C=270mA/g), while the capacity retention after long-term cycling was still outstanding at 1C (1C=270mA/g) (from 0.8% to 80.8% after 500 cycles) as shown in Figure S6 (e) and (f). The issue of voltage decay in high voltage $LiCoO_2$ is proposed for the first time, especially at 4.6V. It is widely believed that voltage decay is mainly due to progressive structural rearrangement, including irreversible transition metal migration. Regarding Co, the reduction from one redox couple to another involves different orbitals, and the Co^{2+}/Co^{3+} redox couple involves the loss (oxidation) or addition (reduction) of electrons in the spin-up e_g orbitals. However, the Co^{3+}/Co^{4+} redox couple involves the loss (oxidation) or addition

(reduction) of electrons in the spin-down t_{2g} orbital[10b, 19]. In addition, the reduced polarization will lead to the midpoint voltage remaining at the original level in the cycling process. Therefore, the migration and reduction of Co, and the resultant formation of Co_3O_4 on the surface are the main reasons for voltage decay. In contrast, the voltage decay of LM0.01COF0.02 is significantly suppressed, which corresponds to capacity retention due to the decrease in irreversible oxygen escape after MgF_2 doping. The galvanostatic charge/discharge curves of both samples are shown in Figure S6 (c) and (d) and are indicative of the suppressed voltage decay in the LM0.01COF0.02 samples. The voltage decay in the Bare-LCO samples is caused by structural changes and the migration of Co through oxygen vacancies due to lattice oxygen release, but the voltage decay in the LM0.01COF0.02 sample is well inhibited, which indicates that tailoring the Co3d band center and the O2p band center can also inhibit the voltage decay in the high voltage $LiCoO_2$ cathode material. In contrast, we also investigated the effect of the amount of doped MgF_2 on the electrochemical performance. The cycling performances of the LM0.02COF0.04, LM0.03COF0.06, LM0.01CO and LCOF0.02 samples at 1C are also worse than that of the LM0.01COF0.02 sample as shown in Figure S6 (e) and (f). We also found that the LM0.01COF0.02 cathode materials exhibit a lower polarization and stronger reversibility than the other materials. As shown in Figure 2(f), the Bare-LCO cathode materials have almost no capacity after approximately 200 cycles, but the capacity retention of the LM0.01COF0.02 sample significantly increases to 86.4% after 1000 cycles at 5C (a higher current density). A large charge/discharge capacity means that

Li^+ can rapidly insert/extract into the host structure while maintaining the stability of the layered structure. The cycling performances of the LM0.02COF0.04 and LM0.03COF0.06 samples at 5C are also worse than that of the LM0.01COF0.02 sample as shown in Figure S6 (h). The role of the Mg "pillar" can also reduce coulomb repulsion in the transition metal interlayer due to the excessive decrease in the amount of Li^+, and the strain and stress on the lattice caused by Li^+ extraction are also alleviated, not only providing an efficient Li^+ migration channel for Li^+ intercalation/extraction but also benefitting the structural stability and cycling performance.

In addition to the cycling performance at 4.6V, the cycling stability in the voltage range of 3.0V~4.5V is also tested at 0.02C and 1C as shown in Figure S7 (a) and (b). Although the initial capacity is not as high as that of the Bare-LCO sample, the capacity retention of the LM0.01COF0.02 sample (0.2C: 82.13% VS 96.35% after 100 cycles; 1C: 69.3% VS 91.6% after 500 cycles) is largely improved. Therefore, the LM0.01COF0.02 cathode material can maintain excellent cycling stability in the voltage range of 3.0~4.5V and 4.6V due to the Mg "pillar" and stability of oxygen in the host structure. We also compared our results with those previously reported, which show that the LM0.01COF0.02 sample co-doped with MgF_2 has super-competitive electrochemical performance as shown in Table S9. Therefore, this material has outstanding cycling stability, and the capacity retention is the highest in the articles reported thus. Electrochemical impedance spectroscopy (EIS) and the potentiostatic intermittent titration technique (PITT) were tested to further reveal the reasons for the excellent electrochemical performance as shown in Figure S8 (c) ~ (f). Compared with

the Bare LCO electrode materials, the values of Rs and Rp are much lower for the LM0.01COF0.02 electrode materials due to MgF_2 doping, and the Li^+ diffusion coefficient is also improved as shown in Figure S8 (e) and (f). In addition, the migration energy barriers of both samples were investigated by DFT calculations. Compared with the Bare-LCO cathode materials, the migration barrier of the LM0.01COF0.02 samples decreases from 0.39eV to 0.29eV as shown in Figure S8 (g), which indicates rapid Li^+ diffusion, corresponding to the improvement in the rate capacity[20].

To further reveal the mechanism of oxygen redox, the O1s XPS spectra of both samples was obtained at the original and state of charge. As shown in Figure S9, compared with the Bare LCO sample, the ratio of lattice oxygen in the LM0.01COF0.02 sample improves significantly, which indicates that the structural stability is greatly enhanced. Moreover, it was found for the first time that there is an irreversibility capacity loss in the first cycle of $LiCoO_2$ cathode materials, especially at a high voltage of 4.6V, which is closely related to its electrochemical mechanism (charge compensation mechanism). Figure S10 (a) and (d) reveals the first charge/discharge curves of the Bare LCO and LM0.01COF0.02 samples. The Bare LCO cathode materials exhibit a charging capacity of 279mAh/g and a discharging capacity of 242mAh/g with a coulombic efficiency of 86.7%. In contrast, the as produced LM0.01COF0.02 sample demonstrates electrochemistry activity, shows a charging capacity of 251mAh/g and discharging capacity of 228mAh/g, leading to the coulombic efficiency of 90.8%, and the charge profile of the LM0.01COF0.02 sample is a sloping curve without any plateau, which illustrates that the irreversible charge compensation

platform of the oxygen-ion is obviously suppressed.

In Figure S10 (b) and (e), after charging to 4.6V, compared with the etching to 50nm in Figure S10 (c) and (f), the O_2^{n-} ratio on the surface of the Bare LCO sample is significantly less than that of the LM0.01COF0.02 sample before etching, which indicates that the surface oxygen in Bare LCO is lost in the form of O_2 gas[21], and the irreversibility of the oxygen redox is obvious, while the LM0.01COF0.02 sample still maintains a larger O_2^{n-} ratio indicating that the stability of O_2^{n-} is enhanced by MgF_2 doping. Therefore, the oxygen loss is much less than that of the Bare LCO sample, which is consistent with the DEMS data shown in Figure 3 and indicates that the oxygen redox activity is inhibited, and that the reversibility is enhanced due to MgF_2 doping. Therefore, O_2^{n-} can be well stabilized in the bulk structure, and oxygen redox proceeds reversibly during the charge/discharge processes due to the existence of F^- and its being more electronegative than oxygen[22]. The electrostatic attraction to electrons is stronger, thus, oxygen redox can be inhibited and the purpose of reversible charge compensation can be achieved, which is consistent with the excellent capacity retention, especially at a high voltage of 4.6V. The effective modulation of the O2p orbital and the decrease in the irreversible oxygen redox can stabilize the framework structure of the cathode materials, especially the stability of oxygen on the sample surface.

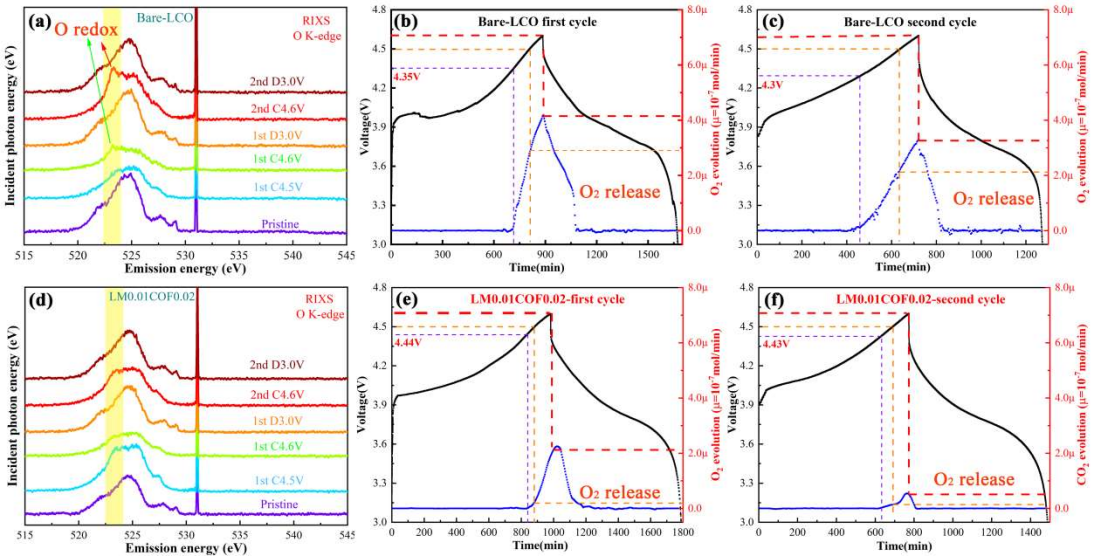

Figure 3 RIXS O K-edge of the Bare LCO (a) and LM0.01COF0.02 (d) samples, respectively, with the excitation energy of 531eV. Operando DEMS of the Bare LCO and LM0.01COF0.02 samples, respectively. The current density is 0.05C. The active materials of the Bare LCO and LM0.01COF0.02 samples is 20.48mg and 25.944mg, respectively, Bare LCO (b) the first cycle, (c) the second cycle; LM0.01COF0.02 (e) the first cycle, (f) the second cycle

Effective detection of lattice oxygen activity requires new techniques that are more sensitive to the chemical state of lattice oxygen[23]. To experimentally probe the nature of oxidized oxygen at different charging states in the Bare-LCO and LM0.01COF0.02 samples, O K-edge RIXS was performed as shown in Figure 3 (a) and (d). Both the Bare-LCO and LM0.01COF0.02 samples show similar features in thier pristine form and discharge state. However, in the charge state, the feature that the oxygen redox activity ($O^{2-} \rightarrow O_2^{n-}$) is more or less constant for the LM0.01COF0.02 samples after two cycles, while it clearly increases for the Bare-LCO. This indicates that oxygen redox in the particle shell of the LM0.01COF0.02 sample is less involved in the chemical

reaction. Improved oxygen stability is reported to help enhance the safety behavior of the cathode material at high voltage, especially at 4.6V[5, 24]. This further supports the idea that the LM0.01COF0.02 cathode material has superior oxygen redox stability, compared with the Bare-LCO sample. Furthermore, element doping has been shown to change the intrinsic electronic structure of the cathode material and consequently affect its oxygen redox chemistry during the lithiation/delithiation process.

Moreover, operando differential electrochemical mass spectrometry (DEMS) measurements of the initial and second charge/discharge processes for the Bare-LCO and LM0.01COF0.02 samples were obtained to reveal O_2 gas loss as shown in Figure 3 (b), (c) and (e), (f), respectively. Compared with the Bare-LCO samples, the loss of O_2 in the bulk structure of the LM0.01COF0.02 electrode materials is well inhibited, which is consistent with the inhibition of the oxygen redox by tailoring the Co3d and O2p band center. Combined with the RIXS data, the enhanced reversibility of oxygen redox can be better revealed. Especially in the second cycle, the release of O_2 in the LM0.01COF0.02 cathode materials decrease significantly, while the release of O_2 in Bare LCO is still very high. The oxidation and release of oxygen are attributed to the generated energy band overlapping between the Co3d and O2p electron orbitals, which leads to the instability of O^{2-}, thus, it is easy to lose electrons at high voltage (versus Li/Li^+) charge states[25]. However, the band overlap of the LM0.01COF0.02 electrode materials is further reduced by MgF_2 doping due to the synergy (the electron extraction from O^{2-} is well inhibited and the Co redox activity is improved) of Mg and F at higher voltages.

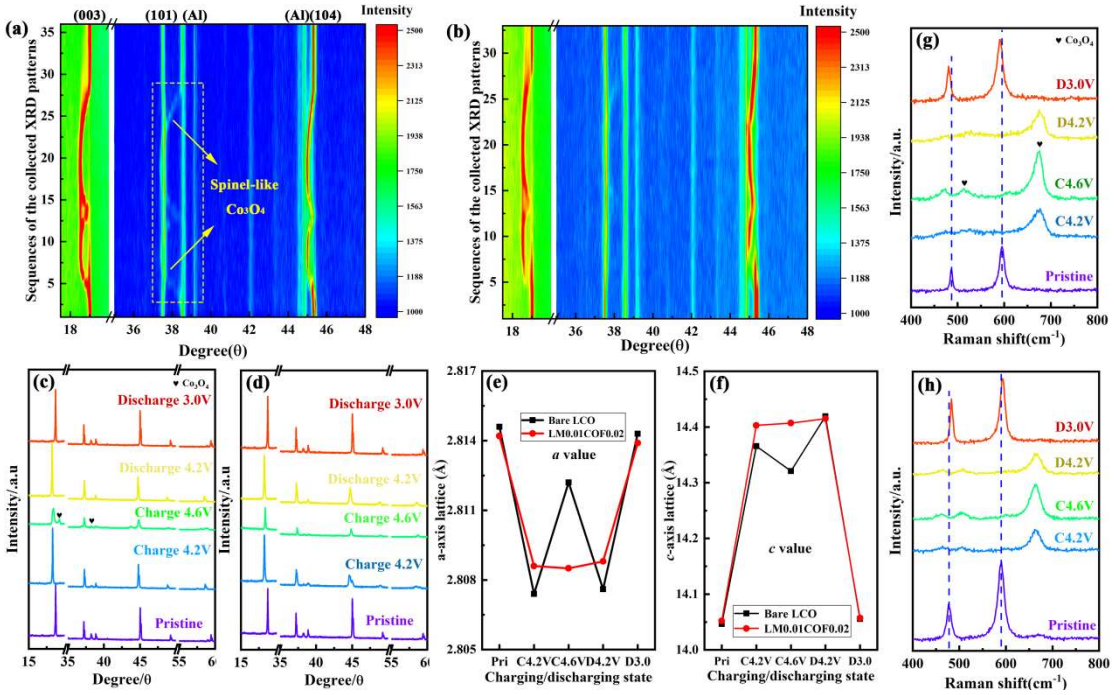

Figure 4 *In-situ* XRD patterns collected during the cyclic voltammograms at 3.0-4.6V with the scan rate of 0.2 mV/s: (a) Bare LCO; (b) LM0.01COF0.02; *Ex-situ* XRD patterns during the first charging/discharging progress; (c) Bare LCO; (d) LM0.01COF0.02; the comparison of the crystal parameters variation (e) the a-axis lattice; (f) the c-axis lattice; *Ex-situ* Raman patterns: (g) Bare LCO and (h) LM0.01COF0.02

To further elucidate and understand the structural effect of MgF_2-doping on the electrochemical performance, *in-situ* XRD and *ex-situ* XRD measurements were performed on Bare-LCO and LM0.01COF0.02 samples. The Bragg reflection (most of the diffraction peaks shift with delithiation/lithiation) shows that the structural evolution of the two samples is quite different during the charge/discharge processes as shown in Figure 4 (a), (b) and (c), (d). Compared with the LM0.01COF0.02 sample, regardless of the data of the first charge/discharge cycle or the second cycle shown in Figure S11 (a) and (b), more spinel Co_3O_4 generated on the surface of the Bare-LCO

sample during the charge/discharge processes, especially at 4.6V, which is consistent with the XPS spectra of the O1s peaks after charging at 4.6V (more irreversible surface spinel Co_3O_4 is formed due to the initial precipitation of a large amount of surface oxygen). The variation in the crystal parameters fluctuates greatly in the Bare LCO sample, while the change of the parameters of the LM0.01COF0.02 sample are very slight as shown in Figure 4 (e) and (f), especially when charged to a high voltage of 4.6V, which illustrates that the harmful phase transition from the O3 hexagonal phase to the hybrid O1-O3 hexagonal phase is inhibited and the structural stability is further enhanced. Almost no obvious spinel Co_3O_4 forms on LM0.01COF0.02 because the inhibition of oxygen escape decreases the migration of the Co ions, which is due to the decrease in the O2p band center and the increase in the energy gap between the Co3d and O2p band centers.

To find the direct evidence of the formation of spinel Co_3O_4 on the surface during the charge/discharge processes, ex-situ Raman spectra were obtained, as shown in Figure 4 (g) and (h). The formation of Co_3O_4 is a reversible process for both the Bare-LCO and LM0.01COF0.02 samples at the first charge/discharge cycle, which indicates the reversibility of the cationic migration during the Li^+ intercalation/extraction process. However, the position of the Raman peak shifts in different directions, compared with the pristine state of both samples. The two Raman characteristic peaks of the Bare-LCO cathode materials at the D3.0V state shift to the left. This indicates the formation of lithium vacancies in Bare-LCO due to O_2 release and spinel phase Co_3O_4 formation, which possibly results from Co migration. A small amount of Co migration to Li sites

will form spinel phase Co_3O_4 to hinder the migration of lithium. In contrast, the peaks in the LM0.01COF0.02 sample shift to the right, which occurs because of the inhibited activity and enhanced reversibility of oxygen redox. These experimental results agree very well with the DFT calculations.

Electronic Structure Analysis

Due to the limitation of Raman spectroscopy, we can only obtain indirect evidence from the surface vibration, which cannot reflect the changes in the chemical environment around Co atoms. Therefore, the evolution of the electron and local structure of Co was studied by combining ex-situ XANES and XPS during the first cycle as shown in Figure S12 and S13. Compared with the Bare-LCO samples, during the first cycle of the charge/discharge processes, the redox activity of the Co-ion in the LM0.01COF0.02 sample is obviously activated, especially when the discharge voltage reaches the lower state. The XANES spectra are more sensitive to local chemical and structural changes, Figure S13 (b) clearly shows that the distance between the Co-O and Co-Co bonds is shortened after the first cycle, which can be attributed to the existence of unfilled lithium vacancies in the lithiation process,[26] this result corresponds to the ex-situ Raman patterns. Moreover, the variation of the Co-O bond is obvious and irreversible in the Bare-LCO sample as shown in Figure S13 (b), but it is reversible in the LM0.01COF0.02 sample as shown in Figure S13 (e), which also reflects that the reversibility of oxygen redox improves and that oxygen escape is inhibited by MgF_2 doping. These results are also consistent with the cyclic voltammetry (CV) curves in Figure 2(a) and (b). Figure S13 (c) and (f), provide the ex-situ XPS data during the first and second cycles. The position of the main Co2p3/2 peaks shift to

higher binding energies in the LM0.01COF0.02 sample after charging to 4.6V obviously, and the positions of the first and second cycles shows no change, in contrast, the Bare-LCO sample changes greatly due to the phase transition and surface cationic densification (the formation of spinel Co_3O_4 on the surface) caused by serious O_2 release and irreversible cationic migration. These results indicate that the redox activity and reversibility of Co ions are further improved, which is beneficial for the enhancing of the Co-O ionic character due to the expansion of the energy band between the Co3d and O2p band centers.

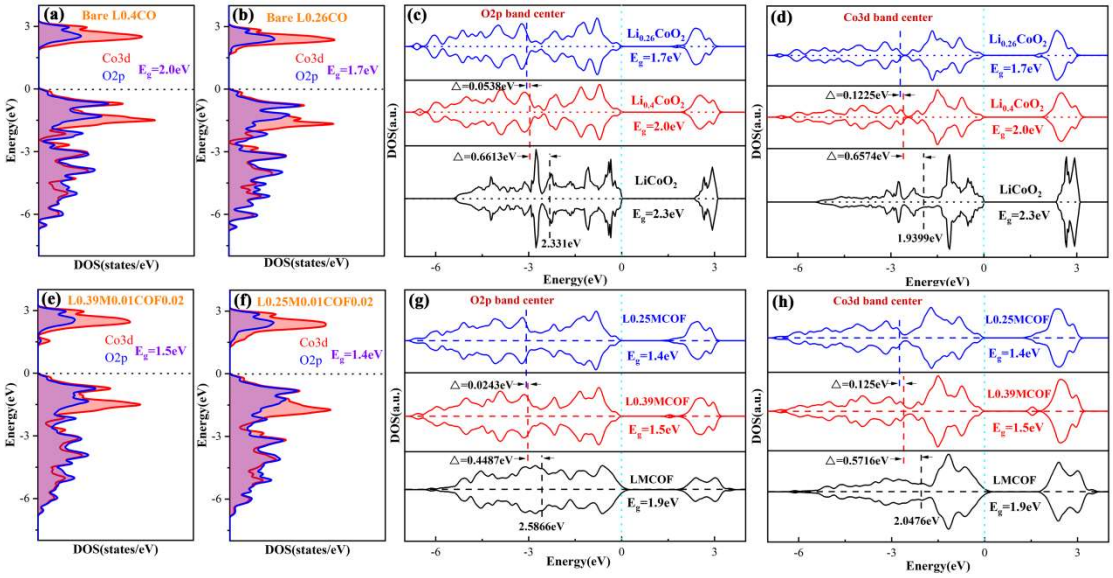

Figure 5 The calculated projected density of states (DOS) and the change of band center with the amount of Li extraction ($Li_{1-x}CoO_2$, x≈0.6 corresponding with charged 4.5V, x≈0.74 corresponding with charged 4.6V), Projected density of states (pDOS) for (a) Bare L0.4CO, (b) Bare L0.26CO, Bare LCO at different lithium content: (c) the O2p DOS, (d) the Co3d DOS; Projected density of states (pDOS) for (a) L0.39M0.01COF0.02, (b) L0.25M0.01COF0.02, LM0.01COF0.02 at different lithium content: (g) the O2p DOS, (h) the Co3d DOS.

To theoretically reveal the effects on the local electronic structure of electrode materials, the DFT method was used to examine the local structure and quantity of oxygen redox of Li^+ extracted from $LiCoO_2$ as shown in Figure 5. Similar to previous studies reported by others, we emphasize that a the high-level hybrid functional was employed, which has been found to be very important for accurately reproducing the electronic structure of oxygen states[27]. Compared with the Bare-LCO samples, for both the charged 4.5V and charged 4.6V samples, the band gap decreases because the edge states of the MgF_2-doped sample appears near the Fermi level, which indicates an improvement in the electrical conductivity and further facilitates charge transfer for rapid kinetics at high voltage. In contrast, the variations in the O2p and Co3d band centers at different states are shown in Figure 5 (c), (d) and (g), (h), respectively. Compared with the Bare LCO sample, there are fewer unoccupied O2p orbitals with a lower energy in the LM0.01COF0.02 sample, which can reduce the probability of the internal charge transition of O^{2-} and further enhances the stability of the oxygen skeleton on the surface of cathode materials, especially after Li^+ extraction. The electronic structure analysis from DFT calculations shows that the stability of oxygen redox is enhanced by the MgF_2 co-doping strategy, which is consistent with the experimental RIXS and DEMS results. Consequently, the structural stability of the LM0.01COF0.02 cathode material is enhanced, which improves capacity retention after long-term cycling. The doping of elements may change the intrinsic electronic structure of cathode materials, thus affecting their redox reactions during charge/discharge processes, especially oxygen redox.

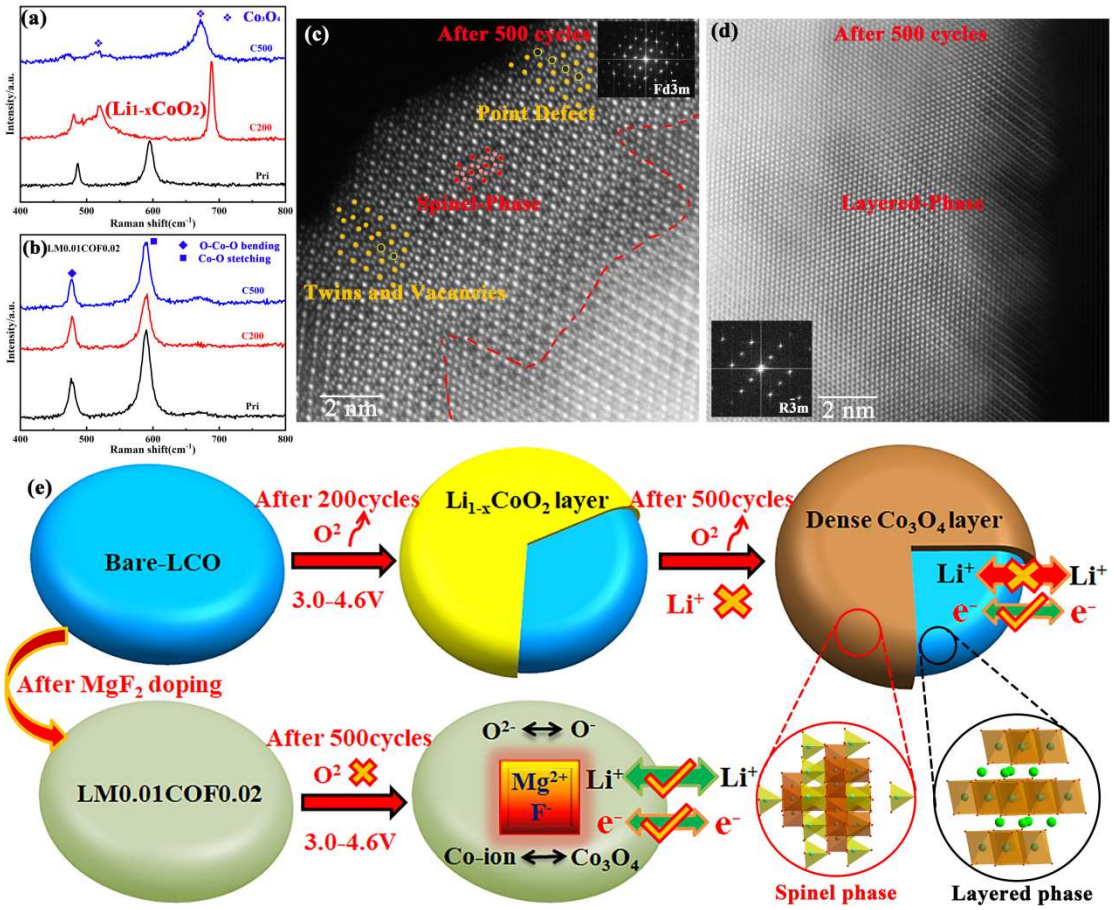

Figure 6 The Raman patterns (a) Bare LCO and (b) LM0.01COF0.02 collected before and after (200, 500) cycles at 1C; the comparison of HAADF-STEM image: (c) Bare LCO: showing Co3O4-like spinel phase (the insert FFT image indicates the spinel phase); (d) LM0.01COF0.02: showing layered structure phase (the insert FFT image indicates the layered structure phase) after 500 cycles at 1C; (e) the proposed performance degradation mechanism schematic diagram of high voltage $LiCoO_2$ cathode materials (different from the previous degradation mechanism of layered structure collapse caused by excessive Li^+ migration).

To clarify the reasons for the improvement in the long-term electrochemical performance after MgF_2 doping, the structural transformation of the Bare-LCO and LM0.01COF0.02 cathode materials was studied before and after 200 or 500cycles as

shown in Figure S14 (a) and (c), respectively. In Figure S14 (a), compared with the pristine state of the Bare-LCO sample, the (003) peak has a significantly shift to the left as well as the characteristic peaks of a hexagonal-layered structure: the (006) and (102) peaks undergo obvious changes after 200 and 500 cycles, which represent the variation in the lattice parameters and damaged layered structure due to O_2 release and the formation of spinel Co_3O_4. However, owing to the inhibition of oxygen escape by the lower O2p band center and the larger energy gap between the Co3d and O2p band centers, the positions of the (003), (006) and (102) peaks of the LM0.01COF0.02 cathode materials hardly change.

The Raman data show that the Co ion in the transition metal layer will occupy the oxygen vacancy by Li^+ extraction during the charging process, and further form spinel Co_3O_4 with an increase in the number of cycles. With increasing lattice oxygen being oxidized and released in the form of O_2 gas, the formation of Li^+-insulator spinel e Co_3O_4 on the surface of cathode materials and the gradual formation of a dense lattice layer (hindering the Li^+ migration) are the main reasons for the rapid decay in high voltage capacity. When cycling to 200 cycles, the surface disorder of the Bare-LCO sample increases, and the typical O-Co-O bending (Eg) and Co-O stretching vibration gradually weaken and finally disappear while a new Co-O stretching vibration appears, which represents the vibration in $Li_{1-x}CoO_2$[28]. When reaching 500 cycles, a new vibration attributed to Co_3O_4 appears on the surface due to continuous lithium migration, as shown in Figure 6 (a), which is consistent with the HAADF-STEM images in Figure 6 (c). It is widely constructed into a Co_3O_4 like spinel structure (space group Fd $\bar{3}$m,

4-8nm thick after 500cycles) in the form of a phase transformation after cycling accompanied by defects: twins and vacancies, which are caused by O_2 escape and the dissolution of Co-ions due to excessive oxygen participating in the redox reaction. It is well known that Co_3O_4 has a normal spinel structure with tetrahedral Co^{2+} and octahedral Co^{3+}, its compact structure and small interstitial sites impede Li^+ intercalation/extraction[29]. Thus, the migration of Li^+ becomes increasingly difficult due to the existence of spinel Co_3O_4 on the surface. However, electrons continue to be transferred, which leads to the constant expansion and inflation of the crystal structure and the random length of the Co-O bond. Therefore, the cathode material will crack or even break during long-term cycling due to the formation of surface Co_4O_3 caused by oxygen release. However, the MgF_2 doped LM0.01COF0.02 cathode materials still maintain their original (complete and orderly) layered structure of hexagonal layered $LiCoO_2$ after 200 and 500 cycles as shown in Figure 6 (b) and (d), respectively, which indicates that the reversibility of cationic migration is enhanced by MgF_2-doping. Moreover, as shown in Figure S14 (d), there is no formation of spinel Co_3O_4 on the surface due to inhibited oxygen redox and the reversibility of Li^+ intercalation/extraction during the charge/discharge process, which leads to a high capacity retention at a high voltage 4.6V. In addition, the cracks and breakages caused by the stress and strain of Li^+ migration all appear in Bare LCO but not in the LM0.01COF0.02 samples, as evidenced in Figure S15, which compares the of the SEM images after 200 and 500 cycles.

As shown in Figure S16, we also analyzed the change in the lattice parameters in

both the Bare-LCO and LM0.01COF0.02 samples before and after 500 cycles by Rietveld refinement. The variations in the lattice parameters: *a*, *c*, and V values are summarized in Tables S10 and S11. The variation rates of *a*, *c* and V for Bare-LCO are 0.2, 1.64 and 1.23%, respectively. In contrast, the variation rates of the lattice parameters *a*, *c* and V for LM0.01COF0.02 significantly decrease to 0.02, 0.03 and 0.01%, respectively, representing an almost "zero strain". These results indicate that MgF_2 doping not only alleviates the lattice stress and strain, but also enhances the stability of the layered structure. On the other hand, the improvement in the structural stability can attributed to F having stronger electronegativity than O, which is consistent with the DFT results. Because more Co-F ionic bonds will lead to a more stable anti-3d orbital of Co after F substituted for O[30], the redox energy of Co will decrease to a favorable energy level compared with the Fermi level and the energy gap between the Co3d and O2p band centers will be further expanded. The inhibited oxygen redox activity and enhanced ionicity of the Co-O bond are also the main reasons for the significantly better electrochemical performance.

Figure 6 (e) shows a schematic diagram for the performance degradation mechanism of high voltage $LiCoO_2$ cathode materials, which is different from the previous degradation mechanism of layered structure collapse caused by excessive Li^+ migration. Oxygen loss can lead to irreversible phase transformations and increasing number of Li^+ vacancies form in the cathode materials, from $LiCoO_2$ to $Li_{1-x}CoO_2$, and become spinel Co_3O_4 with an increase in the number of cycles, thus, spinel Co_3O_4 will accumulate layer by layer. With the increase in the number of cycles, the formation of

Co_3O_4 on the cathode material surface is also an important factor that affects the cycling performance of $LiCoO_2$ materials. It is well known that the spinel Co_3O_4 can inhibit the diffusion of Li^+, especially the migration of Li^+. Furthermore, Li^+ migration can be completely stopped when the compact Co_3O_4 layer is thick enough to cover all the $LiCoO_2$ materials, resulting in a sharp increase in impedance.

Overall, the modulation mechanism of the MgF_2 doping on the $LiCoO_2$ cathode materials was revealed based on the experimental techniques and DFT calculations. Firstly, the electronegativity of F^- is stronger than that of O^{2-} which reduces thickness of $S_{(MO2)}$ and expands the channel of $Li_{(LiO2)}$. This has a profound influence on the structural stability and migration of Li^+ ions in cathode materials. Secondly, Mg acts as a "pillar", providing a stable and enlarged channel for the fast Li^+ intercalation/extraction. Thirdly, MgF_2 doping tailors the Co3d and O2p band center and enlarges their band gap, which reduces the activity of the oxygen redox and inhibits the oxygen escape of $LiCoO_2$ at 4.6V. The inhibition of oxygen escape suppresses the formation of Li-insulator Co_3O_4 and maintains the surface structure integrity. Fourthly, the ionicity of the Co-O bond and the redox activity of Co is enhanced as well as the cationic migration reversibility is improved. For oxide cathode materials, the stability of the oxygen under a high voltage is one of the most prominent issues[31]. The participation of the oxygen in the charge compensation process will lead to a series of undesirable problems such as irreversible O_2 release, phase transition, voltage decay, and the formation of CEI film on the surface of the cathode materials. The proposed modification strategy in this study can also be applied in some other oxides cathode

materials. This study is in progress.

3. Conclusion

In summary, the degradation mechanism of high voltage $LiCoO_2$ was revealed, and we proposed a new strategy to inhibit oxygen escape and improve the reversibility of Co redox (ionicity of Co-O bonds and the reversibility of Co-ion migration was enhanced) by decreasing the O2p band center and tailoring the energy gap between the O2p and Co3d band centers. This not only reduced O_2 escape but also effectively inhibited the harmful phase transition at a high voltage, which further improved the reversibility of cationic migration. Moreover, inhibiting the formation of Co_3O_4 on the surface caused by lattice oxygen release improved the reversibility of Li^+ and e^- intercalation/extraction, which further decreased the lattice strain and stress to prevent cracks and breakages. The Mg "pillar" and the stronger electronegativity of F provided a stable and smaller energy barrier channel for Li^+ migration during the charge/discharge processes. The cooperation of all these effects significantly improved the cycling stability and rate capability of high-voltage $LiCoO_2$ cathode materials without voltage decay especially at 4.6V. The modified $LiCoO_2$ cathode material shows great potential for use in the future commercial applications because of its excellent cycling stability at 4.6V.

Acknowledgements

This work was supported by National Natural Science Foundation of China (Grant No. 11975238, 22005302 and 11575192), the Scientific Instrument Developing Project (Grant No. ZDKYYQ20170001), the Strategic Priority Research Program

(Grant No. XDB28000000) and the International Partnership Program (Grant No. 211211KYSB20170060 and 211211KYSB20180020) of the Chinese Academy of Sciences, of the Chinese Academy of Sciences. This work was also supported by the Fundamental Research Funds for the Central Universities and the China Postdoctoral Science Foundation (2020M680648).

Conflict of interest The authors declare that they have no conflict of interest.

Reference

[1] a) M. S. Whittingham, *Chem. Rev.* **2014**, 114, 11414-11443; b) M. Li, J. Lu, Z. Chen, K. Amine, *Adv. Mater.* **2018**, 30, e1800561.

[2] a) L. Wang, B. Chen, J. Ma, G. Cui, L. Chen, *Chem. Soc. Rev.* **2018**, 47, 6505-6602; b) J. B. Goodenough, K. S. Park, *J. Am. Chem. Soc.* **2013**, 135, 1167-1176; c) J. W. Choi, D. Aurbach, Nat. Rev. Mater. 2016, 1, 16013; d) D. H. Seo, J. Lee, A. Urban, R. Malik, S. Kang, G. Ceder, *Nat. Chem* **2016**, 8, 692-697.

[3] a) X. Wang, X. Wang, Y. Lu, *Ind. Eng. Chem. Res.* **2019**, 58, 10119-10139; b) W. Li, B. Song, A. Manthiram, *Chem. Soc. Rev.* **2017**, 46, 3006-3059; c) F. Wu, J. Maier, Y. Yu, *Chem. Soc. Rev.* **2020**, 49, 1569-1614.

[4] a) L. Wang, J. Ma, C. Wang, X. Yu, R. Liu, F. Jiang, X. Sun, A. Du, X. Zhou, G. Cui, *Adv. Sci.* **2019**, 6, 1900355; b) S. Kalluri, M. Yoon, M. Jo, S. Park, S. Myeong, J. Kim, S. X. Dou, Z. Guo, J. Cho, *Adv. Energy Mater.* **2017**, 7, 1601507.

[5] J.-N. Zhang, Q. Li, C. Ouyang, X. Yu, M. Ge, X. Huang, E. Hu, C. Ma, S. Li, R. Xiao, W. Yang, Y. Chu, Y. Liu, H. Yu, X.-Q. Yang, X. Huang, L. Chen, H. Li, *Nat. Energy* **2019**, 4, 594-603.

[6] J. Qian, L. Liu, J. Yang, S. Li, X. Wang, H. L. Zhuang, Y. Lu, *Nat. Commun.* **2018**, 9, 4918.

[7] Z. Zhu, H. Wang, Y. Li, R. Gao, X. Xiao, Q. Yu, C. Wang, I. Waluyo, J. Ding, A. Hunt, J. Li, *Adv. Mater.* **2020**, 32, 2005182.

[8] Y. Huang, Y. Zhu, H. Fu, M. Ou, C. Hu, S. Yu, Z. Hu, C. T. Chen, G. Jiang, H. Gu, H. Lin, W. Luo, Y. Huang, Angew. Chem. **2020**, 32, 2005182.

[9] J. Li, C. Lin, M. Weng, Y. Qiu, P. Chen, K. Yang, W. Huang, Y. Hong, J. Li, M. Zhang, C. Dong, W. Zhao, Z. Xu, X. Wang, K. Xu, J. Sun, F. Pan, *Nat. Nanotech.* **2021**, 16, 599-605.

[10] a) X. Ren, X. Zhang, Z. Shadike, L. Zou, H. Jia, X. Cao, M. H. Engelhard, B. E. Matthews, C. Wang, B. W. Arey, X. Q. Yang, J. Liu, J. G. Zhang, W. Xu, *Adv. Mater.* **2020**, 32, e2004898; b) D. Ensling, G. Cherkashinin, S. Schmid, S. Bhuvaneswari, A. Thissen, W. Jaegermann, *Chem. Mater.* **2014**, 26, 3948-3956; c) E. Hu, Q. Li, X. Wang, F. Meng, J. Liu, J.-N. Zhang, K. Page, W. Xu, L. Gu, R. Xiao, H. Li, X. Huang, L. Chen, W. Yang, X. Yu, X.-Q. Yang, *Joule* **2021**, 5, 720-736.

[11] a) X. Liu, Y. Tan, W. Wang, C. Li, Z. W. Seh, L. Wang, Y. Sun, *Nano Lett.* **2020**, 20, 4558-4565; b) M. Yoon, Y. Dong, Y. Yoo, S. Myeong, J. Hwang, J. Kim, S. H. Choi, J. Sung, S. J. Kang, J. Li, J. Cho, *Adv. Funct. Mater.* **2019**, 30, 1907903.

[12] E. Hu, X. Yu, R. Lin, X. Bi, J. Lu, S. Bak, K.-W. Nam, H. L. Xin, C. Jaye, D. A. Fischer, K. Amine,

X.-Q. Yang, *Nat. Energy* **2018**, 3, 690-698.

[13] a) Q. Liu, X. Su, D. Lei, Y. Qin, J. Wen, F. Guo, Y. A. Wu, Y. Rong, R. Kou, X. Xiao, F. Aguesse, J. Bareño, Y. Ren, W. Lu, Y. Li, *Nat. Energy* **2018,** 3, 936-943; b) Y. Xu, E. Hu, K. Zhang, X. Wang, V. Borzenets, Z. Sun, P. Pianetta, X. Yu, Y. Liu, X.-Q. Yang, H. Li, *ACS Energy Lett*. **2017**, 2, 1240-1245.

[14] a) J. Chen, W. Deng, X. Gao, S. Yin, L. Yang, H. Liu, G. Zou, H. Hou, X. Ji, *ACS nano* **2021**, 15, 6061-6104; b) R. Gu, R. Qian, Y. Lyu, B. Guo, *ACS Sustain. Chem. Eng*. **2020**, 8, 9346-9355; c) Q. Lin, W. Guan, J. Zhou, J. Meng, W. Huang, T. Chen, Q. Gao, X. Wei, Y. Zeng, J. Li, Z. Zhang, *Nano Energy* **2020**, 76, 105021; d) C. Zhang, Y. Feng, B. Wei, C. Liang, L. Zhou, D. G. Ivey, P. Wang, W. Wei, *Nano Energy* **2020**, 75, 104995.

[15] a) K. Nie, X. Sun, J. Wang, Y. Wang, W. Qi, D. Xiao, J.-N. Zhang, R. Xiao, X. Yu, H. Li, X. Huang, L. Chen, *J. Power Sources* **2020**, 470, 228423; b) W. Kong, D. Zhou, D. Ning, W. Yang, d. wong, J. Zhang, Q. Li, J. Yang, C. Schulz, X. Liu, *J. Electrochem. Soc*. **2021**, 168, 030528.

[16] a) X. Liu, L. Zhang, Y. Zheng, Z. Guo, Y. Zhu, H. Chen, F. Li, P. Liu, B. Yu, X. Wang, J. Liu, Y. Chen, M. Liu, *Adv. Sci*. **2019**, 6, 1801898; b) D. A. Kuznetsov, J. Peng, L. Giordano, Y. Román-Leshkov, Y. Shao-Horn, *J. Phy. Chem. C* **2020**, 124, 6562-6570.

[17] a) L. Xue, S. V. Savilov, V. V. Lunin, H. Xia, *Adv. Funct. Mater*. **2018**, 28, 1705836; b) N. Wu, Y. Zhang, Y. Guo, S. Liu, H. Liu, H. Wu, *ACS appl. Mater. interfaces* **2016**, 8, 2723-2731.

[18] a) K. Liu, S. Tan, J. Moon, C. J. Jafta, C. Li, T. Kobayashi, H. Lyu, C. A. Bridges, S. Men, W. Guo, Y. Sun, J. Zhang, M. P. Paranthaman, X.-G. Sun, S. Dai, *Adv. Energy Mater*. **2020**, 10, 2000135; b) J. W. Fergus, *J. Power Sources* **2010**, 195, 939-954.

[19] a) S. Li, K. Li, J. Zheng, Q. Zhang, B. Wei, X. Lu, *J. Phy. Chem. Lett*. **2019**, 10, 7537-7546; b) D. Eum, B. Kim, S. J. Kim, H. Park, J. Wu, S. P. Cho, G. Yoon, M. H. Lee, S. K. Jung, W. Yang, W. M. Seong, K. Ku, O. Tamwattana, S. K. Park, I. Hwang, K. Kang, *Nat. Mater*. **2020**, 19, 419-427.

[20] a) X. Dai, A. Zhou, J. Xu, B. Yang, L. Wang, J. Li, *J. Power Sources* **2015**, 298, 114-122; b) Y. Wang, Q. Zhang, Z. C. Xue, L. Yang, J. Wang, F. Meng, Q. Li, H. Pan, J. N. Zhang, Z. Jiang, W. Yang, X. Yu, L. Gu, H. Li, *Adv. Energy Mater*. **2020**, 10, 2001413.

[21] N. Yabuuchi, K. Yoshii, S. T. Myung, I. Nakai, S. Komaba, *J. Am. Chem. Soc*. **2011**, 133, 4404-4419.

[22] K. Luo, M. R. Roberts, R. Hao, N. Guerrini, D. M. Pickup, Y.-S. Liu, K. Edström, J. Guo, A. V. Chadwick, L. C. J. N. c. Duda, *Nat. Chem* **2016**, 8, 684-691.

[23] a) C. Schulz, K. Lieutenant, J. Xiao, T. Hofmann, D. Wong, K. Habicht, *J Synchrotron Radiat* **2020**, 27, 238-249; b) H. Hafiz, K. Suzuki, B. Barbiellini, N. Tsuji, N. Yabuuchi, K. Yamamoto, Y. Orikasa, Y. Uchimoto, Y. Sakurai, H. Sakurai, A. Bansil, V. Viswanathan, *Nature* **2021**, 594, 213-216.

[24] a) Q. Li, Z. W. Lebens-Higgins, Y. Li, Y. S. Meng, Y. D. Chuang, L. F. J. Piper, Z. Liu, W. Yang, *J. Phy. Chem. Lett*. **2021**, 12, 1138-1143; b) I. Abate, S. Y. Kim, C. D. Pemmaraju, M. F. Toney, W. Yang, T. P. Devereaux, W. C. Chueh, L. F. Nazar, *Angew. Chem*. **2020**, 133, 10975; c) K. Zhou, S. Zheng, F. Ren, J. Wu, H. Liu, M. Luo, X. Liu, Y. Xiang, C. Zhang, W. Yang, L. He, Y. Yang, *Energy Storage Mater*. **2020**, 32, 234-243.

[25] a) J. Lee, J. K. Papp, R. J. Clement, S. Sallis, D. H. Kwon, T. Shi, W. Yang, B. D. McCloskey, G. Ceder, *Nat. Commun*. **2017**, 8, 981; b) S. Ramakrishnan, B. Park, J. Wu, W. Yang, B. D.

McCloskey, *J. Am. Chem. Soc*. **2020**, 142, 8522-8531; c) M. Ben Yahia, J. Vergnet, M. Saubanere, M. L. Doublet, *Nat. Mater*. **2019**, 18, 496-502.

[26] F. Zhang, S. Lou, S. Li, Z. Yu, Q. Liu, A. Dai, C. Cao, M. F. Toney, M. Ge, X. Xiao, W. K. Lee, Y. Yao, J. Deng, T. Liu, Y. Tang, G. Yin, J. Lu, D. Su, J. Wang, *Nat. Commun*. **2020**, 11, 3050.

[27] R. Sharpe, R. A. House, M. J. Clarke, D. Forstermann, J. J. Marie, G. Cibin, K. J. Zhou, H. Y. Playford, P. G. Bruce, M. S. Islam, *J. Am. Chem. Soc*. 2020, 142, 21799-21809.

[28] a) R. Gao, D. Zhou, D. Ning, W. Zhang, L. Huang, F. Sun, G. Schuck, G. Schumacher, Z. Hu, X. Liu, *Adv. Funct. Mater*. **2020**, 30, 2002223; b) Y. Matsuda, N. Kuwata, T. Okawa, A. Dorai, O. Kamishima, J. Kawamura, *Solid State Ionics* **2019**, 335, 7-14.

[29] Y. Huang, Y. Dong, S. Li, J. Lee, C. Wang, Z. Zhu, W. Xue, Y. Li, J. Li, *Adv. Energy Mater*. **2020**, 11, 2000997.

[30] M. E. A. y. de Dompablo, U. Amador, J. M. Tarascon, *J. Power Sources* **2007**, 174, 1251-1257.

[31] X. Yu, *Nat. Energy* **2021**, 6, 572-573.